Low-Cost CW-LFM Radar Sensor at 100 GHz

Beatriz Mencia-Oliva, Jesús Grajal, Omar A. Yeste-Ojeda, Gorka Rubio-Cidre, Alejandro Badolato

Abstract—**This paper presents a *W*-band high-resolution radar sensor for short-range applications. Low-cost technologies have been properly selected in order to implement a versatile and easily scalable radar system. A large operational bandwidth of 9 GHz, required for obtaining high-range resolution, is attained by means of a frequency multiplication-based architecture. The system characterization to identify the performance-limiting stages and the subsequent design optimization are presented. The assessment of system performance for several representative applications has been carried out.**

Index Terms—**Continuous-wave linear-frequency modulated (CW-LFM), high-resolution radar (HRR), micro-Doppler, millimeter wave, radar imaging.**

I. Introduction

HOMELAND security and surveillance applications are increasingly demanding new capabilities for the detection and identification of human activities. Millimeter-wave sensors are ideally suited for these applications because of the properties of waves in these frequency bands. The wavelength is short enough to permit high-level circuit integration and to obtain high spatial resolution by means of small apertures. Furthermore, operation at these frequencies permits the use of large bandwidths, which generally improves the system performance. Unlike other types of sensors, such as infrared or optical, these systems are able to operate at night time, under conditions of low visibility (dust, fog, rain, or mist) and far from the target location.

There is a wide range of potential applications that can be addressed by millimeter-wave systems including, among others, synthetic aperture radar (SAR) and inverse synthetic aperture radar (ISAR) applications [1], [2] in the field of autonomous navigation, landing guidance [3], automatic target recognition (ATR), and classification techniques [4]; the detection and assessment of human activity at critical infrastructures via micro-Doppler signature extraction techniques [5], [6]; adaptive cruise control (ACC) developed by automotive radars to enhance driving safety [7], [8]; foreign object debris (FOD) detection on airport runways [9] and highways [10]; or, environmental monitoring and cloud profiling radars [11]–[13].

The upcoming application of standoff detection is currently carried out in both civil and military assets and checkpoints. The detection of metallic and nonmetallic concealed objects under clothes or inside luggage is possible by using high resolution radars (HRRs) and taking advantage of the high transmissivity of certain materials at these wavelengths [14]. To this end, the scanning of the scene of interest is carried out by the radar systems. 3-D images are obtained as the result of the 2-D mechanical scanning of the antenna subsystem and the third dimension provided by the radar capability of measuring ranges. Millimeter waves present several advantages in comparison with alternative technologies such as X-rays. It is a nonionizing radiation and systems do not require close proximity to analyze the object of interest. Remarkable examples of systems carrying out this application at the millimeter- and submillimeter-wave band are presented in [15]–[17].

On the other hand, niche industrial applications such as underground mining [18], [19] require the imaging of the internal structures of cavities, and for this purpose, they resort to scanning antenna subsystems. The reduced size of apertures, capable of generating narrow beams, and thus, enabling high angular resolution imaging, as well as the good penetration of dust and water vapor of millimeter waves, make this technology a good candidate for such tasks.

This paper describes a low-cost high-bandwidth continuous-wave linear-frequency modulated (CW-LFM) radar sensor designed for multiple applications. Operating in the millimeter-wave band, it is a 100-GHz homodyne prototype made up of a versatile set of low-cost components. A range resolution as high as 1.67 cm is achieved by means of a transmitted bandwidth of 9 GHz. The selected frequency multiplying architecture and hardware versatility allow the system to be used for a wide variety of short-range applications, such as ISAR imaging for ATR, micro-range/micro-Doppler analysis, and 3-D scanning imaging for security, providing a broad range of image modalities. The homodyne architecture has been selected because of its appeal for low-cost and compact CW-LFM radar systems. In addition, the appropriate selection of technologies to attain versatility and cost savings has led to the use of low-cost signal generation based on direct digital synthesis (DDS), which allows the reconfiguration of the transmitted signal in terms of type of waveform, swept bandwidth or central frequency, and commercial-off-the-shelf (COTS) components at microwave frequencies. Finally, the increasing availability of commercial 100-GHz waveguide components at a relatively reduced cost has contributed to the development of a cost-effective prototype. A highly detailed design process and an exhaustive performance assessment are presented, making the system easily reproducible.

TABLE I
OVERVIEW OF W-BAND RADAR SYSTEMS

	f_c (GHz)	Waveform	B (MHz)	ΔR (m)	Application
Huggard *et al.* [12]	94.0275	Sawtooth chirp	-	16-30	Cloud profiling
Guldogan *et al.* [6]	77	Sawtooth chirp	150	1	Micro-Doppler signatures
Brooker *et al.* [19]	94	Sawtooth chirp	250	1.2	Industry & mining
Rangwala *et al.* [20]	94.75	Sawtooth chirp	500	0.3	Helicopter assisted-landing
Johannes *et al.* [3]	94	Sawtooth chirp	1000	0.15	SAR imaging
Van Caekenberghe *et al.* [21]	94	OFDM	2000	0.075	Autonomous landing guidance
Essen *et al.* [4]	94	Sawtooth chirp/SF	4000/800	0.035/19	ISAR imaging
Hantscher *et al.* [22]	97.5	-	3000	0.05	Security pre-screening
Kapilevich *et al.* [23]	94	Sawtooth chirp	6000	0.025	Standoff detection
Present system	100	Sawtooth chirp	9000	0.0167	Multiple purpose

Table I shows some remarkable W-band radar systems that should be compared with the present radar prototype in terms of central frequency (f_c), waveform, bandwidth (B), range resolution (ΔR), and applications. As regards the central frequency, most of these systems work at 94 GHz, which is used for the operation of imaging millimeter-wave radar applications in astronomy, defense, and security within the window of atmospheric attenuation [24] corresponding to the W-band. Frequencies of around 77 GHz are used for automotive cruise control radar. The reported system operates at a central frequency of 100 GHz. In general, radar systems are designed for a specific purpose, which defines the operational system requirements, such as range resolution or maximum radar range. The transmitted waveform, power, and bandwidth are then selected accordingly. As shown in Table I, sawtooth chirp (CW-LFM) is the most widely used waveform in the listed systems, including the radar reported in this paper. The major advantages of using a CW-LFM waveform lie in the requirement for low power levels for continuous-wave operation, which permits a solid-state solution to be developed, as well as diminishes the probability of interception and interference with other systems. In addition, the required signal processing is easy to implement. Nevertheless, there are other systems based on stepped frequency (SF) [25] or orthogonal frequency-division multiplexing (OFDM) [26] that take advantage of the required narrowband processing and the use of digital-implemented architectures, respectively. The present radar uses a large bandwidth of 9000 MHz in comparison with the bandwidths from 150 MHz [6] up to 6000 MHz [23], featuring a significantly high-range resolution. However, the swept bandwidth of 9000 MHz can be easily adjusted so as to meet the requirements of a certain application by the simple reconfiguration of the DDS module. These characteristics and its hardware versatility make the system suitable for multiple applications as opposed to the application-specific radar systems listed in Table I.

The remainder of this paper is organized as follows. Section II describes the structure of the reported radar system. Sections III and IV present a detailed system characterization and the consequent optimization process. Experimental results for several imaging applications are detailed in Section V. Finally, conclusions are drawn in Section VI.

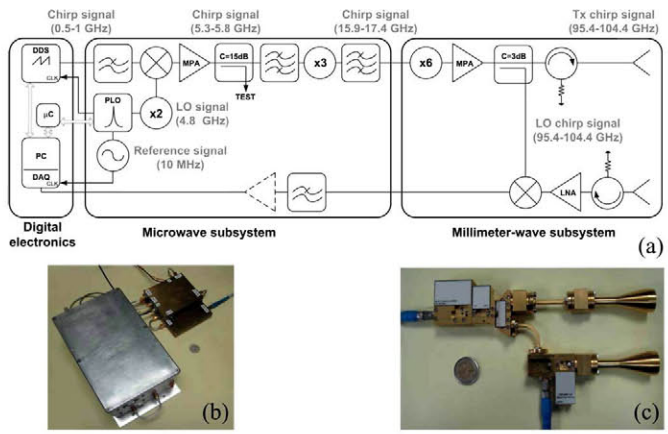

Fig. 1. (a) Simplified block diagram of the radar system. (b) Photograph of signal generation (*left*) and microwave modules (*right*). (c) Photograph of the millimeter-wave subsystem.

II. CW-LFM RADAR SYSTEM

This section deals with the description of the CW-LFM HRR reported in this paper. The detailed block diagram of the 100-GHz radar prototype has been presented in [27]. A simplified version of this diagram is reproduced here in Fig. 1(a), where subdivisions corresponding to the technologies involved in the design have been highlighted. The homodyne configuration has been chosen since it requires a reduced number of components compared to a heterodyne system, in which extra oscillators are usually needed [25].

The maximization of the transmitted bandwidth has been an operational requirement so as to attain high-range resolution. The radar system operates in a bandwidth of 9 GHz, ranging from 95.4 to 104.4 GHz. This bandwidth results in a theoretical range resolution of 1.67 cm, obtained by the well-known expression [28]

$$\Delta R = \frac{c}{2B} \tag{1}$$

where c is the free-space propagation velocity and B is the transmitted bandwidth. However, the main disadvantage of operation on large bandwidths is the great difficulty involved in ensuring the linear performance of the different components over such a large range of frequencies.

The system architecture is based on upconversion and frequency multiplication of a chirp signal generated by DDS. The reason behind the use of this configuration is that the signal bandwidth is directly multiplied by the same multiplication factor, which allows chirp signals to be generated sweeping over large bandwidths in high-frequency bands. In addition, this architecture makes the system easily scalable to higher bands by adding subsequent amplification and frequency-multiplying stages. Nevertheless, it requires close attention to be paid to harmonic and spurious bands at every multiplication stage. Thus, the selection of frequencies is a key task in the prototype design. In the present system, the transmitted bandwidth is centered at 100 GHz instead of 94 GHz. The atmospheric attenuation at 100 GHz is about 0.5 dB/km [24]. It leads to negligible losses due to atmospheric absorption for the intended short-range applications. The range of distances of interest for the radar system operation is from 3 to 30 m.

A. Hardware

As shown in Fig. 1(b) and (c), the radar has been implemented in several modules or subsystems: the signal generation module, the microwave modules, and the millimeter-wave subsystem.

1) Signal Generation: The basis of the radar's signal generation subsystem is a commercial DDS module from Euvis, which ensures the frequency sweep linearity of the transmitted chirp waveform. In addition, its versatility permits the generation of arbitrary frequency chirping waveforms and the easy reconfiguration of signal parameters (swept bandwidth, repetition interval, number of frequency points), while requiring clock frequencies of up to 3 GHz. The development of novel DDS modules, accepting such high clock frequencies, has enabled the generation of chirp signals of unusually large bandwidths located at frequency bands of up to approximately 40% of the clock frequency. This constraint is set in order to ease the subsequent filtering of the alias bands generated by the DDS [29]. If low clock frequencies were used, the chirp signal would ramp over lower frequencies and then additional multiplication stages would be required, which would worsen the phase-noise performance. More precisely, this DDS uses a 2.4-GHz clock frequency to generate a sawtooth chirp signal, ramping from 0.5 to 1 GHz in a maximum repetition interval of 1.5 ms. The minimum repetition interval at 2.4-GHz clock input is 54 ns.[1]

The spectrum of the chirp signal generated by the DDS module is plotted in Fig. 2. Its power level ranges from -2 to -4.5 dBm because the chirp amplitude follows a *sinc* rolloff response, whose first null is located at the clock frequency. The reason behind this fact is the quantized nature of the DDS sampled output [29], which some DDS pre-compensate by means of anti*sinc* filters. In the present case, the DDS does not feature anti*sinc* pre-compensation.

A major drawback of the DDS is the generation of spurious signals on account of its inherently digital nature. To assess the spurious-free dynamic range (SFDR), single tones from 0.5 to 1 GHz have been generated by the DDS and measured by a spectrum analyzer (Fig. 2). From these results, it can be inferred that the SFDR performed by the DDS while using a 2.4-GHz clock signal is roughly 40 dBc.

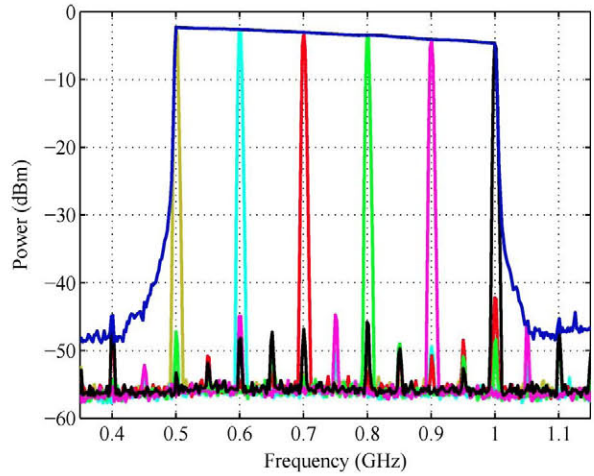

Fig. 2. Chirp signal ramping from 0.5 to 1 GHz in a repetition interval of 1.5 ms, measured at the DDS output. Measurements of single tones from 0.5 to 1 GHz show an SFDR of roughly 40 dBc.

A key component of this subsystem is a commercial 10-MHz oven-controlled crystal oscillator (OCXO) from Oscilloquartz. To address the requirement of coherence and system-wide synchronization, the 10-MHz signal is distributed as the reference signal of the whole system. This fact has motivated the selection of an ultra low phase noise oscillator so as to reduce its impact on the system performance. It is worth mentioning that phase noise is affected by factor $\mathbf{20\log(N)}$ dB, where $\boldsymbol{N}$ is the chain's multiplication factor. The master oscillator signal drives a Synergy 2.4-GHz phase-locked oscillator (PLO), which simultaneously provides the DDS clock signal and, after being doubled, the LO mixer signal for the upconversion process of the DDS output signal. The 10-MHz reference signal is also used as the clock frequency for data acquisition (DAQ). On the other hand, this subsystem also includes a Netburner embedded microcontroller (μC) in charge of the initial configuration of other components. The physical dimensions of this module are $220 \times 140 \times 110$ mm^3 [see Fig. 1(b)].

It is worth noting that, despite having implemented this scheme based on DDS [20], there are alternative configurations for signal generation such as those based on a free-running voltage-controlled oscillator (VCO), whose performance is limited by frequency sweep linearity [30]; or those based on a hybrid DDS/phase-locked loop (PLL), where the DDS provides a chirp signal used as the reference input for the PLL [31]. That closed-loop configuration ensures the linearity of the frequency sweep and it is a good alternative to the selected scheme.

2) Microwave Modules: The rest of the microwave components have been integrated into another two modules in order to avoid electromagnetic interference (EMI)-related problems [see Fig. 1(b)]. They are primarily based on Hittite encapsulated monolithic microwave integrated circuits (MMICs) and other commercial surface-mount technology (SMT) components, assembled on custom-made microstrip technology circuits. These

[1]The minimum waveform length of this DDS module is 16 frequency points for the standard mode of operation. It results in a minimum repetition interval of 54 ns, taking into account that the frequency update rate of this DDS module is 1/8 of the input clock.

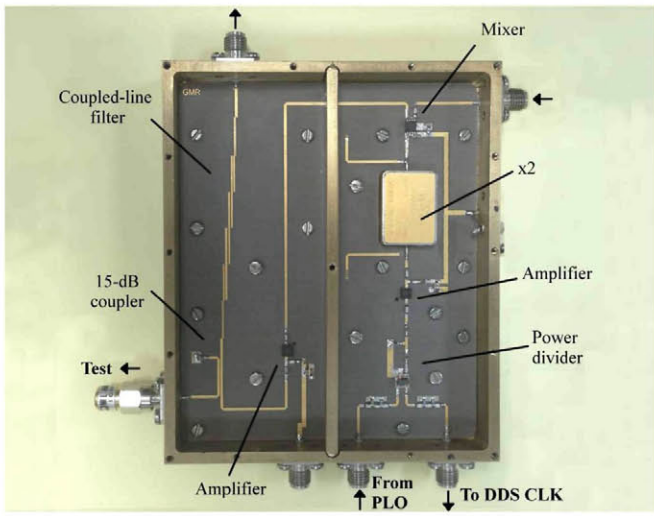

(a)

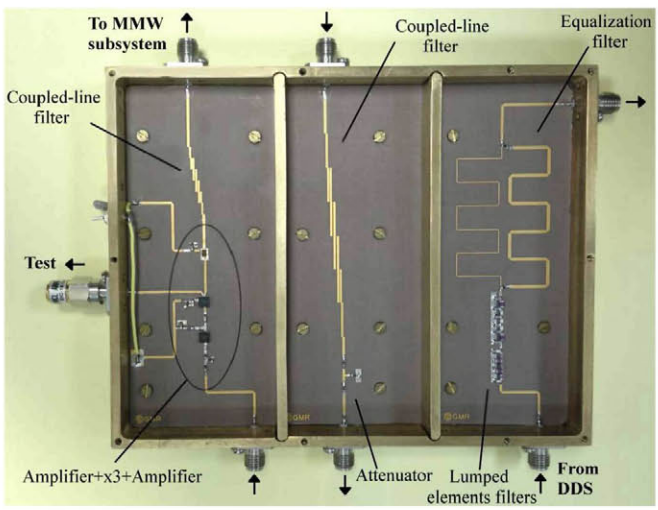

(b)

Fig. 3. Photograph of the microwave modules, which are based on MMICs, SMT components, and in-house microstrip circuits. The dimensions of these modules are: (a) $90 \times 100 \times 20$ mm^3 and (b) $135 \times 100 \times 20$ mm^3, respectively.

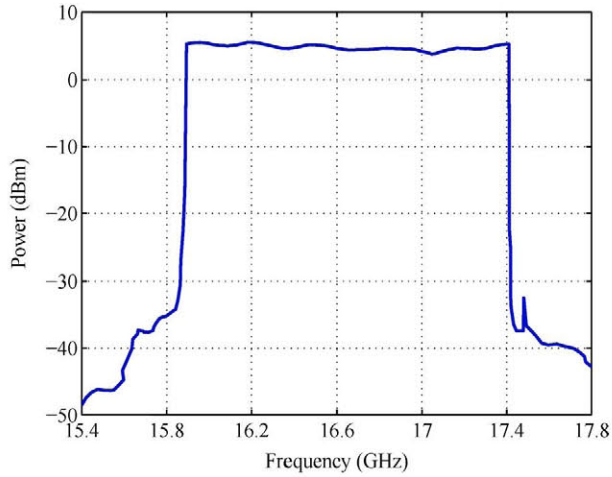

Fig. 4. Chirp signal ramping over 15.9–17.4 GHz measured at the microwave subsystem output.

circuits have been designed by using a commercial CuClad substrate ($\varepsilon_r = 2.17, h = 0.254$ mm) and their performances have been assessed by electromagnetic simulation in ADS Momentum. After the design process, they have been manufactured in-house and individually characterized before their integration. Fig. 3(a) and (b) presents detailed photographs of the integrated modules. As shown, several *ad hoc* coupled-line filters have been designed in the different frequency bands in order to remove the alias bands generated by the DDS, the undesired mixing products, and the harmonic bands resulting from frequency multiplication [see Fig. 1(a)]. In addition, it should be pointed out that an equalization filter [32] has been designed to flatten the amplitude envelope of the chirp signal generated by the DDS [on the right of Fig. 3(b)], which overcomes the lack of inverse *sinc* filter. Other circuits such as a 15-dB coupler for signal test and attenuators for power level adjustment have been also designed and integrated with different MMIC amplifiers and frequency multipliers. The spectrum of the chirp signal at the microwave subsystem output is plotted in Fig. 4, with a maximum ripple of ± 0.9 dB over an average power level of 4.75 dBm.

3) Millimeter-Wave Subsystem: This subsystem is composed of WR-10 waveguide components. At these frequencies, the components are usually designed and implemented in waveguide technology because it is beneficial in terms of maximum power handling, low losses, shock, and corrosion resistance. Some of the components used in this prototype are: an active $\times 6$ frequency multiplier, a medium-power amplifier of gain 10 dB, a power divider, isolators, a low-noise amplifier (LNA) of gain 24 dB and noise figure 3.8 dB, and a 6.5 dB-conversion losses fundamental mixer. The components are commercial items from Radiometer Physics GmbH, except the fundamental mixer, which has been supplied by Quinstar. At this point in the multiplier's chain, the transmitted power is about 9 dBm, ramping over a total bandwidth of 9 GHz. Fig. 5 shows the power measurements at different points of the transmitter's chain. The measurements at W-band have been obtained by means of an Erickson PM4 power meter from Virginia Diodes Inc. The figure clearly shows that the medium power amplifier (MPA) is introducing a ± 2-dB ripple across the band of interest, in agreement with its S-parameter characterization included in its datasheet.

A two-antenna configuration [see Fig. 1(c)] has been used to increase isolation between the transmitter and the receiver, as well as improving the receiver robustness against the phase noise of a short-range target [33]. Picket–Potter horn antennas have been selected for this prototype as a low-cost alternative for corrugated horns at these frequencies. They basically compensate for cross polarization by dual-mode excitation instead of using corrugations. The mechanization of corrugations at 100 GHz requires demanding manufacture processes, increasing considerably the cost of the horn antenna. The chosen dual-mode antennas have a half-power beamwidth (HPBW) of 12°, while return losses are better than 27 dB over the band of interest. Other low-cost radar systems choose the alternative option of using only one antenna for

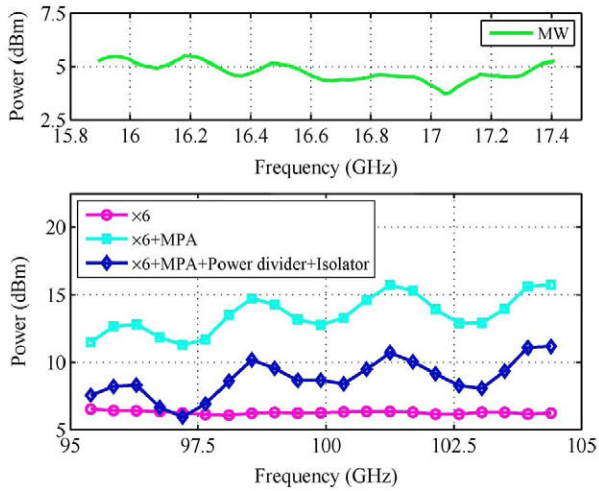

Fig. 5. Power measurements at the output of different components of the transmitter's chain. The input power of the W-band ×6 frequency multiplier corresponds to the power level at the output of the microwave subsystem (*top*). The power measurements at 95.4–104.4 GHz have been obtained by an Erickson PM4 power meter (*bottom*). The system's transmitted power corresponds to the measured power at the isolator's output (diamond marker).

the transmitter and receiver. A circulator is required so as to separate both signals. Typical performance of circulators in the W-band is about 20 dB of isolation in narrow relative bandwidths of approximately 2%. Therefore, only systems intended for narrowband applications can be implemented with this configuration. To overcome this limitation, radar systems for broadband applications can substitute the circulator with a directional coupler, whose performance generally covers the entire W-band. However, this approach has a significant drawback: losing transmitted or received power or both and therefore sacrificing signal-to-noise ratio (SNR). On the other hand, it has to be taken into consideration that reflected power at the antenna input, on account of its finite return losses, would leak into the receiver. This leakage would appear as a powerful short-range target, which would lead to receiver saturation or the masking of other short-range targets, if they are of interest for the particular application. Another solution is to isolate the transmitter and receiver by means of an optical beam splitter [15], which provides increased isolation with regard to a directional coupler, but presents the same problem of loss of power in its standard configuration. In addition, a beam-splitter configuration requires the use of two antennas placed perpendicularly.

As regards the receiver, it is made up of a LNA to reduce the noise figure and a fundamental balanced mixer in charge of the dechirping process. The poor performance of the LNA in terms of its return losses could mean the reradiation of the received power. To avoid this problem, an isolator has been connected at its input [see Fig. 1(a) and (c)] at the expense of slightly worsening the receiver noise figure. The IF signal is low-pass filtered to remove the unwanted mixing products. The estimate of the receiver's noise figure by means of Friis formula results in 4.63 dB, assuming perfect match between the receiver's components [34]. To evaluate how realistic this figure is, a noise budget analysis has been carried out taking into account the scattering

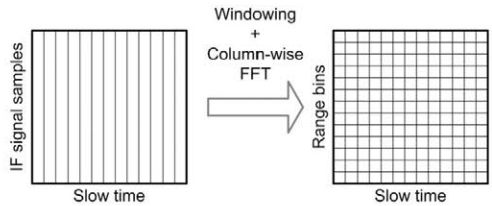

Fig. 6. Processing scheme to obtain the IF signal spectra as a function of slow time. The signal spectrum contains the beat frequencies of the different targets, which can be translated to range by using (2). As a result, the so-called range-slow time matrix is obtained.

and noise parameters of the different devices. For this approach, the resulting receiver's noise figure is 7.88 dB.

B. DAQ and Signal Processing

The resulting IF signal is digitized by a 16-bit digitizer from ADLINK Technology assembled on a conventional personal computer (PC). The sampling frequency is 10 MHz, directly driven by the master oscillator. A sampling rate of 10 MS/s is enough to analyze the retrieved IF signal spectrum, taking into account the range of distances of interest for the radar operation. Signal processing is carried out via standard fast Fourier transform (FFT), as done for most CW-LFM implementations. As a result of the spectral analysis of the IF signal, the locations of the different targets at the scene can be readily obtained from their corresponding beat frequencies f_b by means of the following expression:

$$f_b = \frac{2RB}{cT} \tag{2}$$

where R is the distance at which the target is located, B is the transmitted bandwidth, c is the free-space propagation velocity, and T is the chirp period. The spectrum of a single target with uniform weighting provides the narrowest main-lobe width, and therefore the best range resolution, but high sidelobe levels (SLLs). This characteristic can lead to the concealment of nearby low radar cross-section targets in presence of a powerful target. To tackle this problem, the IF signal can be windowed so as to reduce the SLLs in exchange for a loss in SNR and a main-lobe widening. For applications where a large dynamic range of target reflectivities is expected, such as imaging, weighting functions of low sidelobe performance, such as Hanning or Hamming windows [35], are generally used. The processing scheme is presented in Fig. 6. The IF signal samples corresponding to a chirp period form a column of the first matrix; then, after windowing and applying a column-wise FFT, the range-slow time matrix is obtained where each of its columns is known as a range profile.

C. Overall Considerations

To sum up, the main operational parameters of the system are included in Table II. It is worth mentioning that the overall power consumption is 25 W, which is mainly consumed by the signal generation module. Precisely, 17.7 W is the power consumption of this module while only 2 and 5.3 W are consumed by the microwave modules [see Fig. 3(a) and (b)] and the millimeter-wave subsystem [see Fig. 1(c)], respectively. In this regard, optimization of the subsystems' power consumption will

TABLE II
PARAMETERS OF THE SYSTEM AT 100 GHz

Parameter	Value
Central frequency (f_c)	100 GHz
Bandwidth (B)	9 GHz
Waveform	Sawtooth chirp
Chirp period (T=1/PRF)	54 ns - 1.5 ms
Theoretical range resolution (ΔR)	
Obtained from (1)	1.67 cm
Hanning window at -6 dB	3.33 cm
Transmitted power (P_t)	9 dBm
Radar range (R)	3 m - 30 m
Horn antenna HPBW	12°
Polarization	Linear (horizontal)
Estimated receiver noise figure (NF)	7.88 dB
Sampling frequency (f_s)	10 MHz

TABLE III
ESTIMATE OF THE RADAR SYSTEM COST

Components	Price (€)
Signal generation module	3,500
Microwave modules	500
Waveguide components	21,000
Data acquisition card + PC	2,000

be an important task in the future. The system's overall dimensions are 300 × 275 × 110 mm^3 and its weight is 4 kg.

A preliminary estimate indicates that the cost of the prototype is under €27 000. Table III details the individual cost of each subsystem. The elevated cost of the signal generation subsystem in comparison to the microwave modules is mainly due to the DDS and the ultra-low phase-noise OCXO. Even though the waveguide components at the W-band are already commercially available at relatively low cost, the millimeter-wave subsystem is the major contribution to the overall cost.

III. System Characterization

This section deals with the characterization of the system performance. In this context, several experiments have been carried out in order to measure the radar range resolution, range accuracy, sensitivity, and phase-noise performance. The radar system has been configured to use a chirp period $T = 1.5$ ms, which yields 15 000 samples per chirp period. The data processing comprises Hanning windowing and FFT with zero-padding up to 32 768 points. This radar configuration is used by default unless otherwise stated. A metallic sphere of radius 15 mm (RCS $= -31.5$ dBm) has been chosen as a point-like target in this set of experiments. Some aspects of the system characterization were previously presented in [27], [36], and [37].

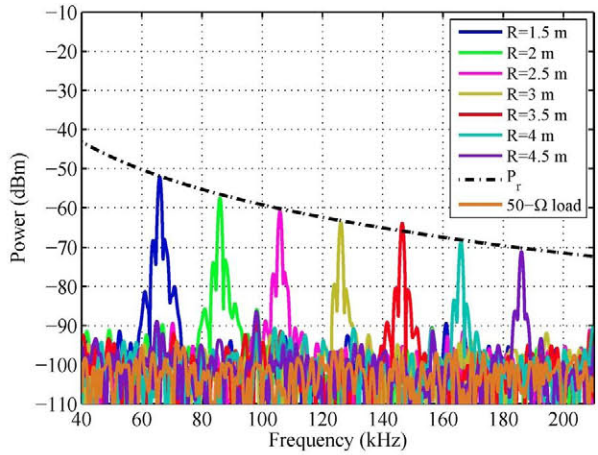

Fig. 7. IF spectra for a metallic sphere of 15-mm radius located at different distances the radar front-end. Each spectrum has been obtained by processing a chirp period of the measured IF signal. According to (3), P_r scales with range as $1/R^4$. The signal captured for a 50-Ω load connected to the digitizer input is also presented. The noise floor for the metallic sphere measurements is approximately that of the digitizer plus some clutter from the indoor environment. This fact proves that dynamic range for these measurements is being limited by the digitizer's quantization noise (see Section III-B).

A. Range Resolution

For imaging systems in general and in imaging radars in particular, a point-like scatterer has a representation given by the so-called point spread function (PSF) of the system. The measurement of a target with known radar cross section (RCS), such as a metallic sphere, is suitable for measuring the PSF. This measurement is equivalent to obtaining the impulse response in linear systems. A straightforward experiment to obtain the PSF of the present system consists of measuring the backscattered signal from the selected metallic sphere located at different positions between 1.5–6 m. For completeness, ranges outside the desired operational range of the radar system (3–30 m) have been selected to carry out this experiment. The results are shown in Fig. 7.

As range resolution can be measured following different criteria, the main-lobe bandwidth at −6 dB for Hanning windowing [35] has been chosen in this paper. This bandwidth is translated into range resolution by means of (2). The range resolution for every target in Fig. 7 is 3.25 cm, better than the expected 3.33 cm (Table II). This effect is likely to be caused by the high-level sidelobes in the PSF and it leads to the need for system calibration. Additionally, Fig. 7 shows the curve of received power obtained by the well-known radar equation [28], which confirms that received power scales with range as $1/R^4$

$$P_r = \frac{P_t G_t G_r \lambda^2 \sigma}{(4\pi)^3 R^4} \tag{3}$$

where P_t is the transmitted power, G_t is the transmitter antenna gain, G_r is the receiver antenna gain, λ is the operational wavelength, and σ is the target's RCS.

B. Sensitivity

The sources of noise that contribute to the limitation of a radar system sensitivity are the transmitter's phase noise, the receiver's thermal noise, and the digitizer's quantization noise. As

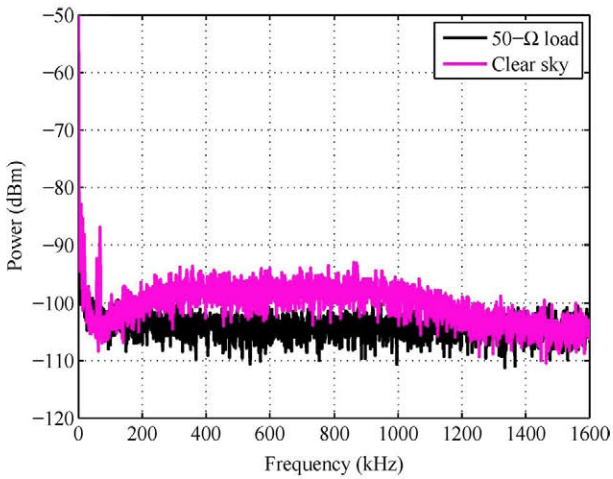

Fig. 8. Measurement of receiver's noise power floor after including an amplifier of gain 22 dB in the receiver's chain. Slow-time noncoherently averaging of 100 consecutive range profiles have been performed so as to reduce noise fluctuations.

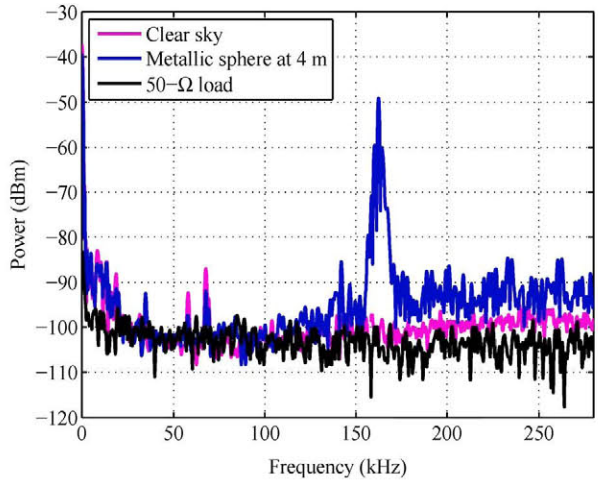

Fig. 9. Measurements of noise power level when a 22-dB gain amplifier is included in the receiver's chain. The receiver's noise floor is higher than the digitizer's, and therefore, the SNR of a specific target is maximized with respect to the case previously presented Fig. 7. Slow-time noncoherently averaging of 100 consecutive range profiles have been performed so as to reduce noise fluctuations.

shown in Fig. 7, the noise floor for the metallic sphere measurements coincides with the signal captured for a 50-Ω load connected to the digitizer input plus some clutter from the environment. The estimated total noise power at the receiver's output is −119 dBm measured over a 1-kHz bandwidth, which corresponds to the bandwidth of an FFT bin (666.6 Hz) affected by a Hanning window [35]. This level is certainly below the digitizer's quantization noise. Therefore, the dynamic range is being limited by the digitizer performance. For instance, the detected SNR for a metallic sphere located at 4 m is 35 dB, in contrast to the theoretical SNR of 50 dB estimated by the radar equation [28].

A well-known technique to solve this problem is to increase the gain of the receiver's chain. An amplifier with 22 dB of gain has been included in the receiver's chain (see Fig. 1 via the dashed line). Fig. 8 shows the spectrum obtained while pointing the radar toward the clear sky when using the 22-dB gain amplifier. The receiver's noise power level can be readily identified above the digitizer's, as well as some spurious signals at 60 and 70 kHz, which were previously hidden by the digitizer's noise floor and fall beyond the band of interest. The receiver's noise spectrum is bandpass as a result of low-pass filtering (see Fig. 1) and high-pass filtering implemented by the decoupling capacitors of the amplifier itself. It filters out the beat frequencies of potential powerful targets located at distances outside the range of interest, as well as the aliasing of noise bands.

To prove the increase in a target's SNR, the IF spectrum of a metallic sphere at 4 m is presented in Fig. 9. The received power of the target has increased by 20 dB, corresponding to the gain of the bandpass amplifier at the target's beat frequency. It is detected SNR is 50 dB, measured as the ratio between received power of the target and receiver's noise floor obtained in the clear sky measurement. This SNR coincides with that estimated with the radar equation. However, the parameter that limits the system's sensitivity is the signal-to-clutter ratio (SCR), which for the metallic sphere at 4 m is approximately 44 dB (Fig. 9).

C. *Range Measurement Accuracy*

The results in Fig. 7 have also unveiled a frequency offset in the measurement of the targets' beat frequency. This frequency offset directly implies the addition of an offset in the measurement of the targets' range, and therefore, uncertainty of the targets' location. To quantify this lack of accuracy in the range measurements, the beat frequencies of the different targets from Fig. 7 have been collected in Fig. 10. Since the targets' positions from the radar front-end are known *a priori*, the theoretical beat frequencies obtained by applying (2) can be compared with the measurements. As shown in Fig. 10, a constant 6-kHz frequency offset is present in every measurement, which is equivalent to an extra 15 cm in range measurement. Its origin lies in the difference between electrical paths of the transmitter and receiver channels, as can be seen in Fig. 1(c). This residual electrical path can be compensated in post-processing by subtracting the frequency offset to the whole data set of measurements.

D. *Phase-Noise Measurement*

Fig. 11 shows the phase-noise performance of the system. It includes phase-noise measurements of a single tone at the central frequency of the bandwidth at the interfaces between technologies [see Fig. 1(a)], i.e., at 750 MHz and 16.65 GHz, respectively. Additionally, the 2.4-GHz signal at the PLO output has also been measured. This batch of measurements has been carried out by using an Agilent N9030A PXA signal analyzer. Due to the lack of W-band measurement equipment, the phase-noise level of the transmitted signal at 100 GHz has been estimated following two different procedures, which are: 1) from the measurement at 16.65 GHz by adding $\mathbf{20\log(N)}$ dB, where $\boldsymbol{N = 6}$ is the corresponding multiplication factor and 2) by adding the phase-noise contributions of the different signals that are the basis of the transmitted signal, i.e., from the measurements at 750 MHz and 2.4 GHz, taking into account the multiplication factor at each stage. Fig. 11 shows that both estimates are in good agreement and represent acceptable values of phase noise

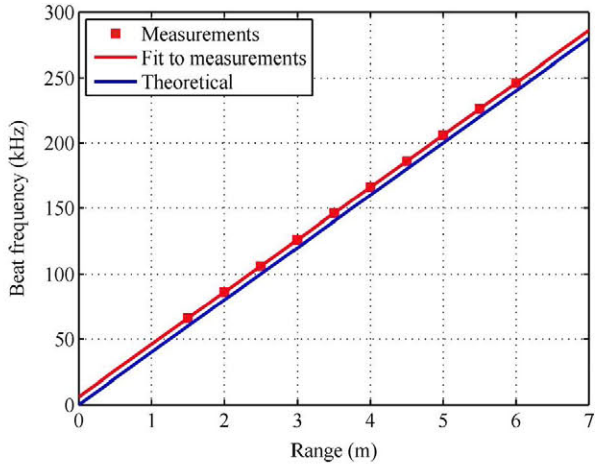

Fig. 10. Measurement of beat frequency as a function of a metallic sphere range. The interception point at 0-m range is 6 kHz and corresponds to the frequency offset present in every target measurement.

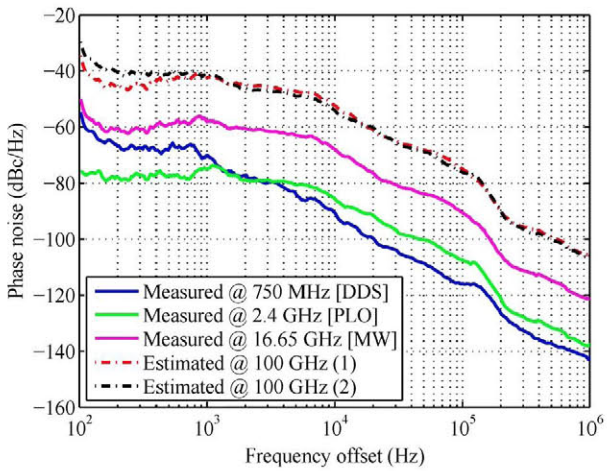

Fig. 11. Phase-noise characterization at different points of the transmitter's chain: measurements at 750 MHz (DDS output), 2.4 GHz (PLO output), 16.65 GHz (microwave subsystem output), and estimates at 100 GHz: (1) from the measurement at 16.65 GHz and (2) from the measurements at 750 MHz and 2.4 GHz.

attained by a low-cost radar system operating in the W-band. For the sake of comparison, integrated VCO-based radars at the W-band such as those reported in [7] and [38] present phase noise values of −98.7 and −88 dBc/Hz at 1-MHz offset from the carrier, respectively, which are at least 8 dB worse than the present system.

IV. Performance Optimization

Taking into account the preliminary experimental results, the following performance optimization has been carried out.

A. Signal Spectral Purity at Different Stages of the System

Results in Section III-A show that the PSF is deformed on account of the nonideal effects produced by radar electronics. In this context, the identification of critical components or subsystems is of great interest in order to optimize the radar system performance. By taking advantage of the scalability of the chosen architecture, it is possible to monitor the linearity and spectral

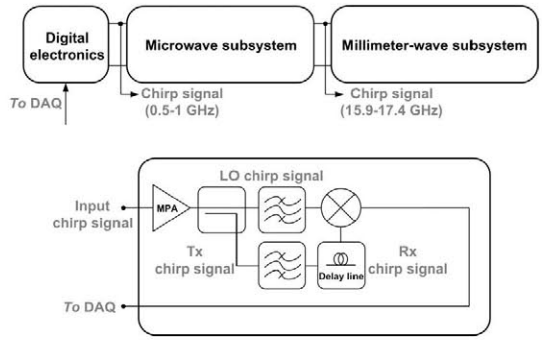

Fig. 12. Simplified scheme of the radar system prototype (*top*) and generic block diagram of the transceivers used to monitor the spectral purity of the transmitted chirp signal at the interfaces between technologies (*bottom*).

purity of the transmitted chirp signal at different stages of the transmitter's chain with simple transceivers. These transceivers for testing are based on general purpose components, in which the antenna subsystem has been suppressed and a point-like target is emulated by means of a delay line between the LO and RF mixer ports. A coaxial cable of known length is generally used to implement this delay line. The generic block diagram is illustrated in Fig. 12 (*bottom*).

In the present radar system, the chirp signals at the interfaces between technologies have been selected to be assessed, as indicated in Fig. 12 (*top*). To this end, two test transceivers have been developed working at 0.5–1 and 15.9–17.4 GHz, respectively. The target has been generated by a coaxial cable of 15 m in length. The resulting PSF of both experiments are compared in Fig. 13 with that obtained at 95.4–104.4 GHz.

The detailed features of the PSF are included in Table IV. The results of the measurements have to be compared with the theoretical range resolution measured at −6 dB ΔR_{th} and the first SLL of −32 dBc [35], provided by the Hanning window when the input signal is a sinusoid. As shown, the PSF in Fig. 13(a) and (b) presents a slightly higher SLL while remaining main-lobe width, and therefore the range resolution, unchanged. These results illustrate that the purity and linearity of the chirp signal have been maintained across the transmitter's chain up to the interface between microwave and millimeter-wave subsystems. Nonetheless, as shown in Fig. 13(c), the PSF obtained at 95.4–104.4 GHz (Section III-A) is considerably degraded in comparison with (a) and (b). From these results, it can be inferred that the main sources of the nonlinear effects and unwanted modulations are commercial W-band frequency multipliers and amplifiers. More precisely, it has been proven by simulation that the amplitude modulation introduced by the MPA (Fig. 5) is to a large extent responsible for the degradation of the PSF [39].

B. Reduction in Nonlinear Effects in Range Resolution by Calibration

As previously explained, the mixer output for a point-like target should be ideally a single tone. From the results of Section III, the system's calibration has to be carried out in order to compensate the deformation of PSF, which consequently is limiting the instantaneous dynamic range. As part of the IF signal post-processing, the calibration process is based

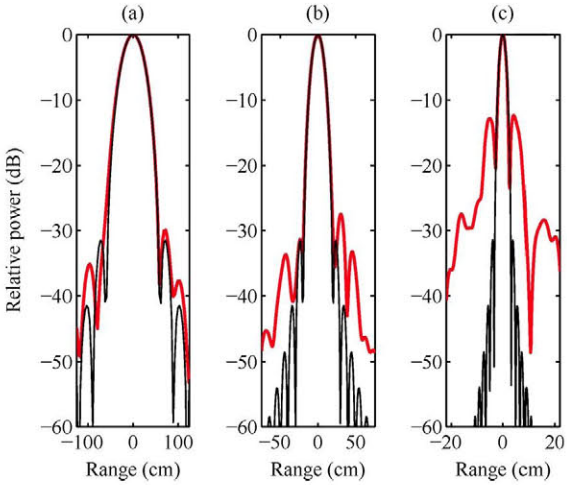

Fig. 13. Results of spectral purity measurements of a point-like target for chirp signals of bandwidth: (a) 0.5–1 GHz, (b) 15.9–17.4 GHz, and (c) 95.4–104.4 GHz. The ideal response is shown in each graph as a reference. Received power and targets' location have been normalized so as to compare the results easily.

TABLE IV
PSF FEATURES AT DIFFERENT STAGES OF THE RADAR SYSTEM

Chirp bandwidth	ΔR_{th}	$\Delta R_{measured}$	$\mathrm{SLL}_{measured}$
0.5-1 GHz	60 cm	60 cm	-30 dBc
15.9-17.4 GHz	20 cm	20 cm	-27.6 dBc
95.4-104.4 GHz	3.33 cm	3.25 cm	-12.3 dBc

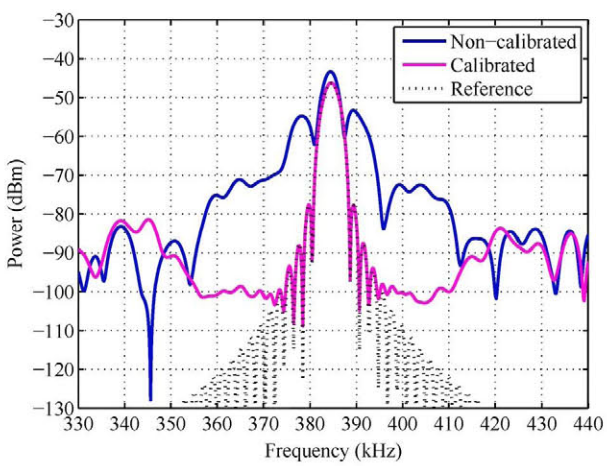

Fig. 14. Self-calibration of a point-like target located at 3.2 m.

on the removal of the unwanted modulations so that the IF signal obtained from a point-like target is a sinusoid [15].

Fig. 14 presents the resulting IF spectrum for the raw signal, the calibrated signal, and the ideal response at the beat frequency of the target as a reference. It should be noted that the chirp period used in this experiment has been $\boldsymbol{T = 0.5}$ ms. The deviation of the uncalibrated signal from the single tone can be readily observed. As a result of the calibration process, the compensated signal is identical to the reference up to the third sidelobes.

To assess the quality of the calibration, the normalized root mean square (rms) calibration error is defined as the difference between the calibrated target and the reference window in the

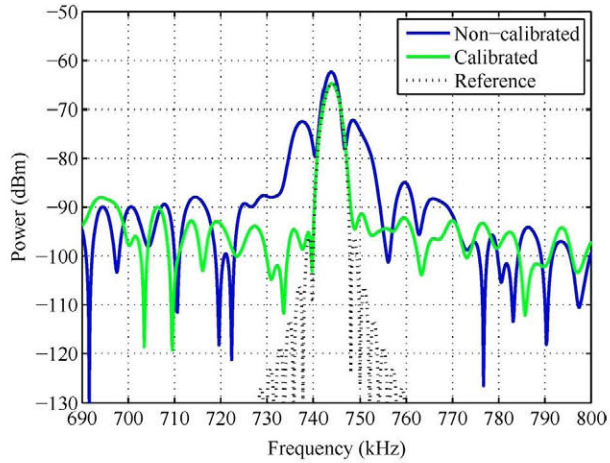

Fig. 15. Results of the calibration process of a target located at 6 m while using the calibration data obtained from a target at 3.2 m (Fig. 14).

TABLE V
NORMALIZED RMS ERROR FOR THE CALIBRATION PROCESS

Target location	Calibration data	Normalized RMS error
3.2 m	Self-calibration	0.0103
4 m	Target at 3.2 m	0.148
5 m	Target at 3.2 m	0.234
6 m	Target at 3.2 m	0.214

vicinity of the target corresponding to its main lobe and first sidelobes. The maximum rms error is considered to be that obtained for the uncalibrated target and it is used to normalize the rms error for the calibrated targets. Thus, the normalized rms error ranges from 0 to 1. As an example, for the target at 3.2 m (Fig. 14), the normalized rms error is 0.0103. In order to give more weight to calibration errors located in the main lobe, this error is computed by using 70% of FFT bins located at the main lobe and 30% at both first sidelobes.

The final objective of this procedure is to obtain the calibration data from a single target located at a certain distance and then to use it to calibrate subsequent measurements independently of the distance of the targets. Fig. 15 presents the results after calibration of a 6-m target by using the data from Fig. 14. The normalized rms error is 0.214. As shown, the responses differ from its reference in the first sidelobes, which are degraded to the noise level of the radar system. After several experiments, it has been observed that the calibration process can be considered valid for normalized rms error values of up to 0.3. This result directly implies that, for the particular case of a 3.2-m point-like target, the obtained calibration data is applicable to targets located up to 7 m. Table V tabulates the results of different calibrated targets in terms of their normalized rms error.

Finally, an experiment has been carried out to further illustrate the benefits of the calibration process. It consists of comparing the range profiles obtained from a single target and two targets spaced 5 cm apart. The nearest target is a metallic sphere of 7.5 mm in radius ($\mathbf{RCS = -37.5}$ dBm) located at 3.95 m, whereas the second one is the previously used sphere of 15 mm in radius ($\mathbf{RCS = -31.5}$ dBm) located at 4 m. Fig. 16(a) plots

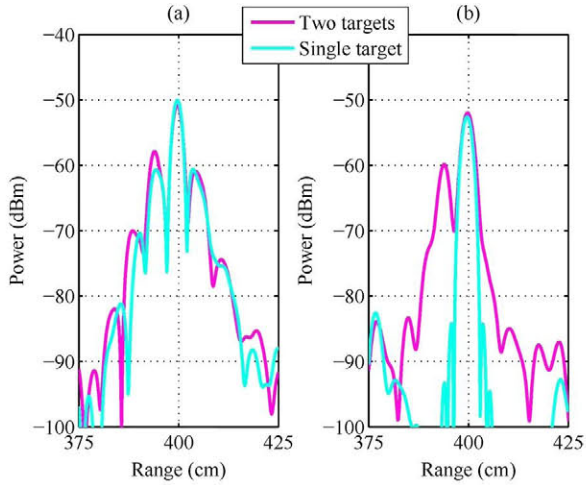

Fig. 16. Range profiles of two targets and a single target: (a) before calibration and (b) after calibration. The calibration data has been obtained from the single target echo. It can be readily identified the necessity of calibration to improve the instantaneous dynamic range.

both range profiles when the signals have not been calibrated and (b) the calibrated range profiles. When the signal is not calibrated, it is impossible to determine how many targets there are in the scene because of the poor dynamic margin. On the other hand, the presence of the nearest target is quite clear after the calibration process.

V. Applications

The system performance has been assessed for different applications in several deployment scenarios while the system architecture remained unchanged.

A. ISAR Imaging for ATR

Experiments for this application are based on locating the target of interest on a rotating platform and retrieving the signal scattered back to the radar's antenna. It is then processed by a digital image formation processor (IFP), which generates an image representation of the target's reflectivity (RCS measurement).

The images are obtained by locating the target on a turntable platform, which rotates at 4 r/min. The structure is covered with several types of millimeter-wave absorber to reduce its influence on the results. Furthermore, the remaining background is removed by suppressing the static targets in the scene throughout the whole DAQ. The data processing is based on the polar formatting algorithm (PFA) and the detailed procedure is described in [27].

The long-term objective is to generate a database of targets reflectivity for ATR, composed of ISAR images of different scaled model targets. Some preliminary experiments have been carried out with a selection of potential targets of interest with the aim of validating the radar system operation for this application. Figs. 17 and 18 show ISAR images and their corresponding photographs of a dump truck and a digger models, these scaled by factor 1:32. These results would be equivalent to those obtained by illuminating the full-size targets with an S-band radar working at 3 GHz, which is the result of scaling 100 GHz by a factor of 32:1. It should be noted that these results have been obtained by placing the scaled models on their side on the turntable platform.

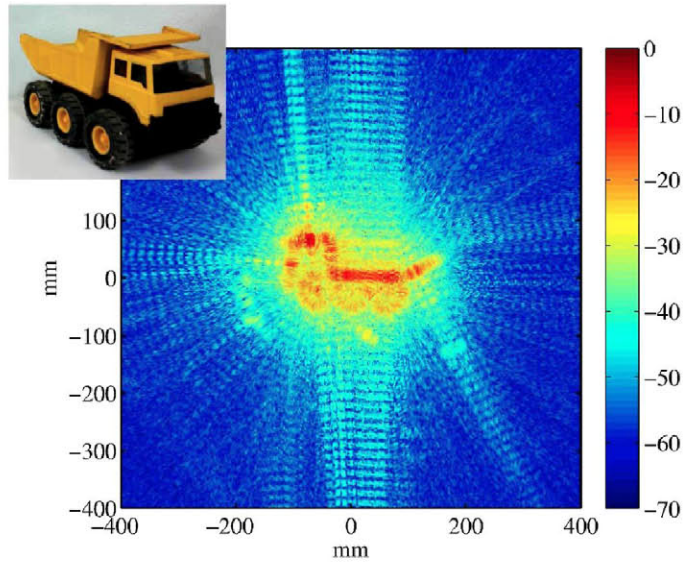

Fig. 17. ISAR image and photograph of a 1:32 scaled dump truck model.

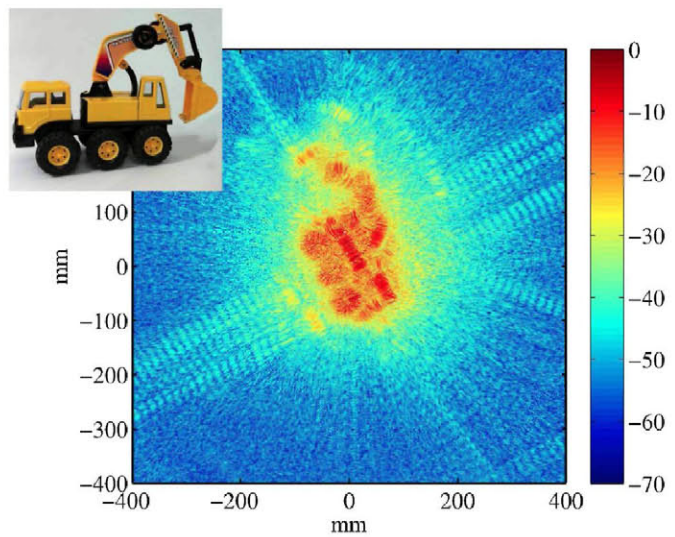

Fig. 18. ISAR image and photograph of a 1:32 scaled digger model.

B. Micro-Range/Micro-Doppler Experiments

Several experiments for micro-range/micro-Doppler analysis of the human body have been carried out. The human gait micro-Doppler signature contains a wealth of information of the target's dynamics, though it tends to be complex due to the effect of scatterer crossings or occlusions. On the other hand, the micro-range analysis allows to resolve scatterers and extract the weakest ones, otherwise hidden. The process involves the analysis of the range-slow time matrix and the spectrogram, obtained from applying the short-time Fourier transform (STFT) to the range-slow time matrix. The processing scheme is detailed in Fig. 19.

The gait signature can be exploited to extract distinctive characteristics from the time-dependent Doppler frequency shifts

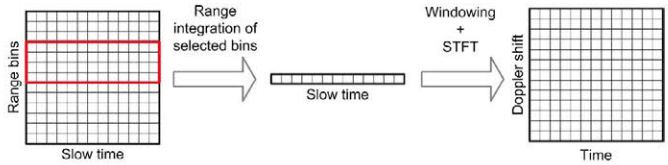

Fig. 19. Processing scheme to obtain the spectrogram representation. From the range-time matrix, the range bins where the target of interest is moving are selected and added along the range dimension; windowing and STFT are applied to the resulting vector, which results in a Doppler shift-time matrix known as the spectrogram of the target.

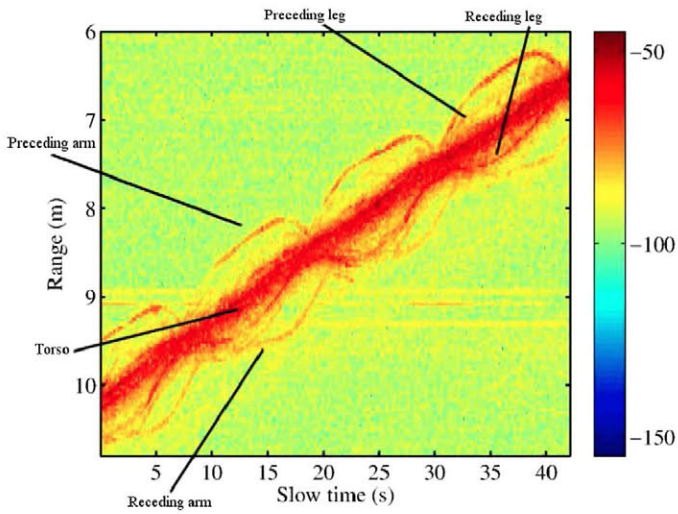

Fig. 20. Range-slow time matrix of a walking person heading for the radar front-end.

produced by vibrations or oscillations of a moving target [5]. The maximum Doppler frequency shift generated by vibrations of frequency f_v and amplitude D_v can be approximated by

$$\max(f_{\text{Doppler}}) = \frac{2}{\lambda} D_v f_v \tag{4}$$

where λ is the wavelength of operation. In this context, the high frequency of this radar prototype is beneficial. In such a high-frequency system, even a very low vibration f_v or very small vibration amplitude D_v can produce significant Doppler frequency shifts that can be readily detected.

As regards the system configuration, several issues have to be taken into account for the selection of the pulse repetition frequency (PRF). PRF determines the sampling rate for Doppler analysis so it must satisfy the Nyquist theorem to avoid ambiguity. Therefore, the range of Doppler frequencies that can be unambiguously measured is $\pm \text{PRF}/2$. The expression for the Doppler frequency [28] as a function of the target radial velocity v_R and the wavelength λ is as follows:

$$f_{\text{Doppler}} = \frac{2v_R}{\lambda}. \tag{5}$$

The experimental setup consists of a person walking, running, heading for, and moving away from the radar location. The average velocity of a human being walking is approximately 5 km/h, which corresponds to torso velocity, and it produces a Doppler frequency shift of 926 Hz at 100 GHz. Nonetheless, arms and legs move faster, demanding the use of PRF values

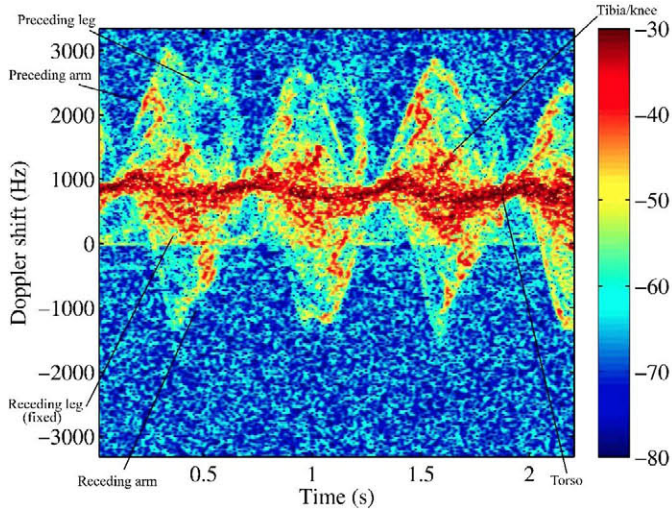

Fig. 21. Spectrogram of a walking person heading for the radar front-end.

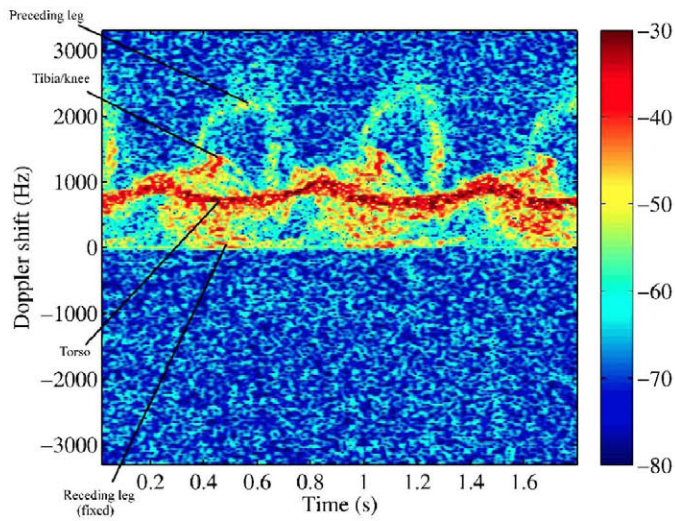

Fig. 22. Spectrogram of a walking person heading for the radar front-end without moving their arms.

greater than 1 kHz. In this particular case, a PRF of 6666 Hz ($T = 0.15$ ms) has been selected to carry out several experiments.

An example of a walking person heading for the radar front-end are presented in Figs. 20 and 21, respectively. A Hamming window has been applied along the range dimension prior to applying the first FFT, and subsequently, along the slow time dimension before performing a 256-point STFT with one-sample displacement between each FFT. It should be noted that the data set has been collected in a controlled indoor environment with negligible Doppler clutter. Static targets have been removed from the scene by suppressing the 0-Hz Doppler bin. In view of Fig. 21, human body parameters such as the torso average velocity of approximately 1000 Hz or motion periodicity of 1.8 cycles/s can be estimated. Additionally, different parts of the human body can be easily identified in conjunction with Fig. 20. However, there are numerous hidden scatterers that cannot be identified as a part of a human body since there is overlap in Doppler frequency and scintillations

over the observation period. Another example of validation of the radar prototype for this application is presented in Fig. 22. It shows the spectrogram of a walking person without swinging their arms. The signatures of legs and torso can be observed clearer than in Fig. 21.

Taking the aforementioned into account, the whole data set may be highly valuable for extracting motion structure and gait parameters estimation, making the recognition of different gait patterns possible [6], [40]–[43].

VI. Conclusion

A millimeter-wave HRR sensor for short-range applications has been presented. A low-cost solution has been implemented while keeping in mind versatility and scalability. The architecture is based on frequency multiplication, which allows large operational bandwidths, and therefore, high-range resolution, to be attained. More precisely, the radar system operates at 100 GHz in a bandwidth of 9 GHz.

The system characterization and the subsequent performance optimization have been addressed in this paper. As a result, the millimeter-wave components have been identified as the most critical in terms of the system's linearity. The characterization of phase noise has proven that good performance can be achieved by low-cost hardware implementations. On the other hand, the dynamic range and the target discrimination capability of the system have been optimized by means of a calibration procedure. Additionally, the system performance has been validated for several short-range applications such as ISAR imaging for ATR and micro-Doppler signature of human gait.

Future work includes the integration of the microwave subsystem achieving a higher level of integration, the optimization of critical components at W-band, or even the substitution of waveguide technology by emerging MMIC technology at 100 GHz. System upgrade in the near future will involve the extension of the radar prototype up to 300 GHz. A $\times 3$ multiplication stage will consequently triple the transmitted bandwidth, and therefore a range resolution of only 5 mm will be achieved. Its integration with a 3-D scanning antenna subsystem will allow the system applicability to be extended to fields such as standoff detection, security, and biomedical applications.

References

[1] M. Soumekh, *Synthetic Aperture Radar Signal Processing With MATLAB Algorithms*. New York: Wiley, 1999.

[2] R. M. M. G. Carrara and R. S. Goodman, *Spotlight Synthetic Aperture Radar Signal Processing Algorithms*. New York: Wiley, 1999.

[3] W. Johannes, H. Essen, S. Stanko, R. Sommer, A. Wahlen, J. Wilcke, C. Wagner, M. Schlechtweg, and A. Tessmann, "Miniaturized high resolution synthetic aperture radar at 94 GHz for microlite aircraft or UAV," in *IEEE Sensors*, Oct. 2011, pp. 2022–2025.

[4] H. Essen, M. Hagelen, A. Wahlen, K. Schulz, K. Jager, and M. Hebel, "ISAR imaging of helicopters using millimeter wave radars," *Int. J. Microw. Wireless Technol.*, vol. 1, pp. 171–178, 2009.

[5] V. Chen, *The Micro-Doppler Effect in Radar, ser. Artech House Remote Sensing Library*. Norwood, MA: Artech House, 2011.

[6] M. Guldogan, F. Gustafsson, U. Orguner, S. Bjorklund, H. Petersson, and A. Nezirovic, "Human gait parameter estimation based on micro-Doppler signatures using particle filters," in *IEEE Int. Acoust., Speech, Signal Process. Conf.*, May 2011, pp. 5940–5943.

[7] S. Nicolson, K. Yau, S. Pruvost, V. Danelon, P. Chevalier, P. Garcia, A. Chantre, B. Sautreuil, and S. Voinigescu, "A low-voltage SiGe BiCMOS 77-GHz automotive radar chipset," *IEEE Trans. Microw. Theory Techn.*, vol. 56, no. 5, pp. 1092–1104, May 2008.

[8] J. Hasch, E. Topak, R. Schnabel, T. Zwick, R. Weigel, and C. Waldschmidt, "Millimeter-wave technology for automotive radar sensors in the 77 GHz frequency band," *IEEE Trans. Microw. Theory Techn.*, vol. 60, no. 3, pp. 845–860, Mar. 2012.

[9] P. Feil, W. Menzel, T. Nguyen, C. Pichot, and C. Migliaccio, "Foreign objects debris detection (FOD) on airport runways using a broadband 78 GHz sensor," in *38th Eur. Microw. Conf.*, 2008, pp. 1608–1611.

[10] K. Sarabandi and E. Li, "Polarimetric characterization of debris and faults in the highway environment at millimeter-wave frequencies," *IEEE Trans. Antennas Propag.*, vol. 48, no. 11, pp. 1756–1768, Nov. 2000.

[11] J. Mead, A. Pazmany, S. Sekelsky, R. Bambha, and R. McIntosh, "Millimeter-wave radars for remotely sensing clouds and precipitation," in *Geosci. Remote Sensing Symp.*, May 1996, vol. 3, pp. 1553–1555.

[12] P. Huggard, M. Oldfield, B. Moyna, B. Ellison, D. Matheson, A. Bennett, C. Gaffard, T. Oakley, and J. Nash, "94 GHz FMCW cloud radar," presented at the SPIE Photo-Opt. Instrum. Eng. Conf., Oct. 2008, vol. 7117.

[13] H. Nakatsuka, T. Kimura, Y. Seki, G. Kadosaki, Y. Iide, K. Okada, J. Yamaguchi, N. Takahashi, Y. Ohno, H. Horie, and K. Sato, "Design and development status of the EarthCARE cloud profiling radar," in *IEEE Int. Geosci. Remote Sensing Symp.*, Jul. 2012, pp. 2415–2418.

[14] R. Appleby and H. Wallace, "Standoff detection of weapons and contraband in the 100 GHz to 1 THz region," *IEEE Trans. Antennas Propag.*, vol. 55, no. 11, pp. 2944–2956, Nov. 2007.

[15] K. Cooper, R. Dengler, N. Llombart, B. Thomas, G. Chattopadhyay, and P. Siegel, "THz imaging radar for standoff personnel screening," *IEEE Trans. Terahertz Sci. Technol.*, vol. 1, no. 1, pp. 169–182, Sep. 2011.

[16] F. Friederich, W. von Spiegel, M. Bauer, F. Meng, M. Thomson, S. Boppel, A. Lisauskas, B. Hils, V. Krozer, A. Keil, T. Loffler, R. Henneberger, A. Huhn, G. Spickermann, P. Bolivar, and H. Roskos, "THz active imaging systems with real-time capabilities," *IEEE Trans. Terahertz Sci. Technol.*, vol. 1, no. 1, pp. 183–200, Sep. 2011.

[17] D. Sheen, D. McMakin, T. Hall, and R. Severtsen, "Active millimeter-wave standoff and portal imaging techniques for personnel screening," in *IEEE Technol. for Homeland Security Conf.*, May 2009, pp. 440–447.

[18] G. Brooker, S. Scheding, M. Bishop, and R. Hennessy, "Development and application of millimeter wave radar sensors for underground mining," *IEEE Sensors J.*, vol. 5, no. 6, pp. 1270–1280, 2005.

[19] G. Brooker, J. Martinez, and R. Hennessey, "Millimetre wave radar imaging of mining vehicles," in *Eur. Radar Conf.*, Oct. 30–1, 2010, pp. 284–287.

[20] M. Rangwala, J. Lee, and K. Sarabandi, "Design of FMCW millimeter-wave radar for helicopter assisted landing," in *IEEE Int. Geosci. Remote Sensing Symp.*, Jul. 2007, pp. 4183–4186.

[21] K. Van Caekenberghe, K. Brakora, and K. Sarabandi, "A 94 GHz OFDM frequency scanning radar for autonomous landing guidance," in *IEEE Radar Conf.*, Apr. 2007, pp. 248–253.

[22] S. Hantscher, B. Schlenther, M. Hagelen, S. Lang, H. Essen, A. Tessmann, A. Hulsmann, P. Leuther, and M. Schlechtweg, "Security pre-screening of moving persons using a rotating multichannel-band radar," *IEEE Trans. Microw. Theory Techn.*, vol. 60, no. 3, pp. 870–880, Mar. 2012.

[23] B. Kapilevich, Y. Pinhasi, M. Anisimov, B. Litvak, and D. Hardon, "FMCW MM-wave non-imaging sensor for detecting hidden objects," in *IEEE MTT-S Int. Microw. Symp. Dig.*, Sep. 2011, pp. 101–104, Workshop ser. Millimeter Wave Integr. Technol..

[24] T. Schneider, A. Wiatrek, S. Preussler, M. Grigat, and R. Braun, "Link budget analysis for terahertz fixed wireless links," *IEEE Trans. Terahertz Sci. Technol.*, vol. 2, no. 2, pp. 250–256, Mar. 2012.

[25] J. Scheer and J. Kurtz, *Coherent Radar Performance Estimation*, ser. Radar Library. Norwood, MA: Artech House, 1993.

[26] C. Sturm, E. Pancera, T. Zwick, and W. Wiesbeck, "A novel approach to OFDM radar processing," in *IEEE Radar Conf.*, May 2009, pp. 1–4.

[27] J. Grajal, B. Mencia-Oliva, O. A. Yeste-Ojeda, A. F. Garcia-Fernandez, and G. Rubio-Cidre, "A prototype of high resolution ISAR imaging system at millimetre-wave band," in *IEEE CIE Int. Radar Conf.*, Oct. 2011, vol. 1, pp. 551–554.

[28] M. Skolnik, *Introduction to Radar Systems*. New York: McGraw-Hill, 1962, ch. 2, pp. 15–67.

[29] "A technical tutorial on digital signal synthesis," Analog Devices, Santa Clara, CA, Tech. Rep., 1999. [Online]. Available: http://www.analog.com/
[30] P. Brennan, Y. Huang, M. Ash, and K. Chetty, "Determination of sweep linearity requirements in FMCW radar systems based on simple voltage-controlled oscillator sources," *IEEE Trans. Aerosp. Electron. Syst.*, vol. 47, no. 3, pp. 1594–1604, Jul. 2011.
[31] P. Almorox-Gonzalez, J.-T. Gonzalez-Partida, M. Burgos-Garcia, B. Dorta-Naranjo, and J. Gismero, "Millimeter-wave sensor with FMICW capabilities for medium-range high-resolution radars," *IEEE Trans. Microw. Theory Techn.*, vol. 57, no. 6, pp. 1479–1486, Jun. 2009.
[32] M. Morgan, T. Newton, B. Hayward, and T. Boyd, "Non-reflective transmission-line filters for gain slope equalization," in *IEEE MTT-S Int. Microw. Symp. Dig.*, 2007, pp. 545–548.
[33] A. Stove, "Linear FMCW radar techniques," *Proc. Inst. Elect. Eng. –Radar and Signal Process.*, vol. 139, no. 5, pt. F, pp. 343–350, Oct. 1992.
[34] S. A. Maas, *Noise in Linear and Nonlinear Circuits*, ser. Microw. Library. Norwood, MA: Artech House, 2005.
[35] F. Harris, "On the use of windows for harmonic analysis with the discrete Fourier transform," *Proc. IEEE*, vol. 66, no. 1, pp. 51–83, Jan. 1978.
[36] B. Mencia-Oliva, J. Grajal, and A. Badolato, "100-GHz FMCW radar front-end for ISAR and 3-D imaging," in *IEEE Radar Conf.*, May 2011, pp. 389–392.
[37] B. Mencia-Oliva, J. Grajal, and O. Yeste-Ojeda, "COTS technologies for radar sensors at millimeter-wave bands," in *IEEE MTT-S Int. Microw. Symp. Dig.*, Sep. 2011, pp. 105–108, Microw. Workshop ser.: Millimeter Wave Integr. Technol..
[38] M. Jahn, R. Feger, C. Wagner, Z. Tong, and A. Stelzer, "A four-channel 94-GHz SiGe-based digital beamforming FMCW radar," *IEEE Trans. Microw. Theory Techn.*, vol. 60, no. 3, pp. 861–869, Mar. 2012.
[39] N. Levanon and E. Mozeson, "Continuous-Wave Signals," in *Radar Signals*. New York: Wiley, 2004, pp. 294–326.
[40] P. van Dorp and F. Groen, "Feature-based human motion parameter estimation with radar," *IET Radar, Sonar Navigat.*, vol. 2, no. 2, pp. 135–145, Apr. 2008.
[41] R. Raj, V. Chen, and R. Lipps, "Analysis of radar human gait signatures," *IET Signal Process.*, vol. 4, no. 3, pp. 234–244, Jun. 2010.
[42] M. Otero, "Application of a continuous wave radar for human gait recognition," pp. 538–548, 2005.
[43] M. Vahidpour and K. Sarabandi, "Millimeter-wave doppler spectrum and polarimetric response of walking bodies," *IEEE Trans. Geosci. Remote Sens.*, vol. 50, no. 7, pp. 2866–2879, Jul. 2012.

Beatriz Mencia-Oliva (S'09) was born in Talavera de la Reina, Toledo, Spain, in 1984. She received the M.Sc. degree in electrical engineering from the Universidad Politécnica de Madrid, Madrid, Spain, in 2008, and is currently working toward the Ph.D. degree at the Universidad Politécnica de Madrid.

Since October 2007, she has been with the Microwave and Radar Group, Department of Signals, Systems and Radiocommunications, Universidad Politécnica de Madrid. Her research interests include the design of millimeter and submillimeter-wave radar systems.

Jesús Grajal was born in Toral de los Guzmanes, Leon, Spain, in 1967. He received the Ingeniero de Telecomunicacion and Ph.D. degrees from the Technical University of Madrid (UPM), Madrid, Spain in 1992 and 1998, respectively.

Since 2001, he has been an Associate Professor with the Signals, Systems, and Radiocommunications Department, Technical School of Telecommunication Engineering, UPM. His research activities are in the area of hardware design for radar systems, radar signal processing, and broadband digital receivers for radar and spectrum surveillance applications.

Omar A. Yeste-Ojeda was born in Sta. Lucía de Tirajana, Las Palmas, Spain, in 1979. He received the Ingeniero de Telecomunicacion and Ph.D. degrees from the Technical University of Madrid, Madrid, Spain, in 2002 and 2007, respectively.

Since 2001, he has been an Associate Professor with the Signals, Systems, and Radiocommunications Department, Technical University of Madrid. His research activities are in the area of signal processing with a special focus on cyclostationarity and time-frequency analysis for signal interception and identification.

Gorka Rubio-Cidre received the B.Sc. degree in telecommunication systems engineering from the University of Málaga, Málaga, Spain, in 2008, the M.Sc. degree in electrical engineering from the Technical University of Madrid (UPM), Madrid, Spain, in 2011, and is currently working toward the Ph.D. degree in communications technologies and systems at UPM.

Since July 2010, he has been with the Department of Signals, Systems and Radiocommunications, UPM. His research interests include signal generation for millimeter- and submillimeter-wave radars and the development of through-the-wall continuous wave (CW) radars at *L*-band for detection and tracking of multiple targets.

Alejandro Badolato is currently working toward the Ingeniero de Telecomunicacion degree at the Technical University of Madrid (UPM), Madrid, Spain.

Since 2010, he has been with the Microwave and Radar Group, Department of Signals, Systems and Radiocommunications, UPM. His interests are in the area of digital electronics design.